The Rigorous Computation of the Molecular Electric Potential

R. J. Zauhar*

Dept. of Physiology and Biophysics, Mount Sinai School of Medicine of the City University of New York, One Gustave Levy Place, New York, NY 10029

R. S. Morgan

Dept. of Molecular and Cell Biology, The Pennsylvania State University, 618 Mueller Bldg., University Park, PA 16802

Received 17 February 1987; accepted 17 July 1987

A method is presented for the rigorous computation of the electric potential of molecules of arbitrary shape, under the assumption of continuous linear dielectric media. The computational technique involves finding the distribution of *induced polarization charge* on the molecular surface, and proceeds by an application of the method of *boundary elements*. The surface, which separates the molecular interior (of low dielectric constant) from the highly polar solvent, is given a piece-wise analytic representation as a collection of curvilinear elements. Given a set of internal fixed charges, the distribution of polarization-charge is found as a continuous function over the surface elements, and the electric potential (including all polarization effects) is then easily computed at any point. The method is applied to a spherical interface, and to several small molecules of biological interest, including a hexapeptide. The resulting potentials show good convergence in all cases. The future application of the method to macromolecules is discussed.

I. INTRODUCTION

The structure and function of biological molecules is determined by the interplay of a variety of forces, involving a number of specific interactions (e.g. van der Waals and dispersion energies between atoms), as well as nonspecific, global influences (such as conformational entropy, and the entropy and enthalpy of hydration). Of these diverse contributions to the free energy of biochemical systems, special attention has been directed to the role of the *electrostatic potential* in determining both the equilibrium structures of biomolecules, and their interaction. Electrostatic forces have been implicated in the capture and binding of substrates by enzymes,[1,2,3] assume a central role in discussions of protein titration,[4,5,6] and are routinely included in simulations of protein dynamics.[7]

While there is general agreement as to the importance of electrostatic interactions in the description of biomolecular behavior, the choice of a methodology for the computation of the molecular electric potential remains problematic. In principle, the total energy of interaction of two solvated molecules can be evaluated (as a function of their relative positions) by microscopic simulations,[8] and similarly, the conformational energy of a single molecule in solution.[9] In practice, such simulations require a great deal of computing time, and involve only a limited number of degrees of freedom for the interacting species. In addition, many interactions of biological interest (e.g. between separated molecules in solution, or between charged side-chains in a protein) are expected to have energies on the order of 1 kcal/mol, and fall within the error of typical Monte Carlo and molecular dynamics calculations.

As an alternative to microscopic simulations, the energy of systems of charged molecules may be approximated by applying classical electrostatic theory. In this approach, the solvent is represented as a continuum, with dielectric constant $D_o \simeq 78$. Solvated molecules are modeled as collections of point charges inside cavities of low dielectric constant $D_i \simeq 1$, embedded in the continuous solvent medium. The resulting potential must satisfy Poisson's equation. While this would appear to be a useful approach, its practical application is hindered by the ab-

*Present address: 519 Biotechnology Institute, University Park, PA, 16802

CCC 0192-8651/88/020171-17$04.00

sence of analytic solutions of Poisson's equation for other than a few simple cavity shapes. The assumption of a spherical solute-solvent boundary (along with introduction of the linearized Poisson-Boltzmann distribution) leads to the classical Tanford-Kirkwood (TK) theory, [10] the first electrostatic model in wide use to explicitly incorporate a dielectric interface between the molecular interior and the surrounding solvent. The TK model (either in its original form, or as modified by Shire et al.[11]) has been used with some success to estimate the pairwise energies of interaction of ionized sites in proteins. However, the form of the electric potential is highly dependent on *which side* of the dielectric interface is being considered, with all electrostatic effects being dramatically reduced as one crosses the dielectric boundary. Thus, for a molecule of arbitrary shape, the conformation of the surface is expected to have a significant effect on the shape of the potential. As a consequence of its geometric constraint, the TK model cannot be used to compute the molecular electric potential in three dimensions for actual protein structures, or to evaluate the electrostatic effects of internal peptide charges.

In an effort to consider molecules of *arbitrary* shape, Warwicker and Watson[12] have introduced a finite-difference method for calculating the electric potential in three dimensions. In their computational scheme, a rectangular grid is superimposed upon the solute-solvent system, partitioning both the molecular interior and the surrounding solvent into small volume elements, with each element assigned the dielectric constant appropriate to its region. The potential is then found by an iterative procedure, given an initial estimate at each grid point. Application of this methodology to proteins has revealed the dramatic influence that molecular geometry may have on the form of the electrostatic potential. However, restrictions on available computing time and storage space have required the use of rather large volume elements (typically 1 Å on a side); as a consequence, it has not been possible to demonstrate convergence of the potential with respect to decreasing grid size, or to perform detailed calculations for surface ionized sites. In a recent application[13] it has been suggested that the method must, at present, be confined to the calculation of long-range electrostatic effects.

To circumvent the difficulties discussed above, we have proposed that the electrostatic potential of biomolecules be calculated by considering the distribution of *induced polarization charge* at dielectric interfaces (rather than by attempting a direct solution of Poisson's equation in three dimensions). As described in our previous article,[14] this approach involves the use of two-dimensional surface elements, in contrast to the requirement of three-dimensional volume elements in the finite-difference method, and permits an order-of-magnitude reduction in the number of elements needed to model a given system. In addition, the polarization-charge technique avoids two difficulties associated with the method of finite-differences: first, the finite-difference method requires that the fixed internal charges coincide with grid points. Given the coarseness of the grids used in practical calculations, this can lead to a serious distortion of the initial charge configuration (although methods have been developed that minimize this problem by distributing fixed charges over several neighboring grid points[15]). In contrast, our approach allows arbitrary charge placement. Secondly the finite-difference method obviously requires a limited number of volume elements, which necessitates the specification of an artificial boundary for the solute-solvent system; no such requirement is met with in the polarization-charge approach.

In our previous article, we described a simple surface-element method for computing the electric potential of proteins. While adequate for preliminary calculations, the methodology involved a crude modeling of the dielectric interface, and was not suitable for a detailed analysis of the molecular potential (as would be required for predicting pK shifts at titratable sites). We now present a more sophisticated model that overcomes the deficiencies of our previous method. Specifically, the dielectric boundary is now represented by a smooth, piece-wise analytic surface, and the induced polarization density is now a continuous function over the surface. We show that convergence of computed potentials is easily achieved for small molecules. The future application to macromolecules is discussed, and

should involve a straightforward extension of the procedures described below.

METHODS

The Concept of Polarization Charge

We represent a solvated molecule by the physical model illustrated in Figure 1. Here, the molecular interior (with dielectric constant D_i) is separated from the solvent medium (with dielectric constant D_o) by an interface S of arbitrary shape. The molecule contains a collection of fixed charges $\{q_k\}$ at positions $\{r_k\}$. While our model will assume *point* charges in the interior, we will temporarily associate with each charge q_k a spherical dielectric interface s_k of finite radius R_c. (This will simplify the incorporation of the internal dielectric constant into our formulation.) The fixed charges will establish a polarization field $P(r)$ throughout the volume of the dielectric medium; it is a well-known result of classical electrostatic theory[16] that the effects of this field can be exactly reproduced by appropriate distributions of *induced polarization charge* at dielectric interfaces. Explicitly, the potential $\Phi(r)$ may be written

$$\Phi(r) = \sum_k \frac{q_k}{|r - r_k|} + \sum_k \left[\int_{s_k} \frac{\sigma_k^c(R) d^2R}{|r - R|} \right] + \int_S \frac{\sigma(R) d^2R}{|r - R|} \quad (1)$$

where $\sigma_k^c(R)$ is the distribution of induced surface charge associated with the spherical interface of the kth charge, and $\sigma(R)$ is the distribution associated with the solute-solvent boundary, S.

To evaluate σ_k^c, we apply the classical relation

$$\sigma_k^c(R) = P \cdot n(R) = \chi_i E \cdot n(R) \quad (2)$$

where R locates a point on the spherical interface s_k, with surface normal n directed away from the molecular interior (i.e. directed toward the center of the fixed charges). P and E are the polarization and electric fields, respectively, at R and just outside the spherical boundary of the charge; χ_i is the dielectric susceptibility of the molecular interior, and is related to D_i by $\chi_i = (1/4\pi) \cdot (D_i - 1)$. The total polarization charge associated with s_k is then found by applying Gauss' law for a dielectric medium,

$$\begin{aligned} q_k^{pol} &= \int_{s_k} \sigma_k^c(R) d^2R \\ &= -\frac{(D_i - 1)}{4\pi D_i} \int_{s_k} D_i |En| d^2R \\ &= -\left\{1 - \frac{1}{D_i}\right\} q_k \end{aligned} \quad (3)$$

where $(D_i E \cdot n)$ is the normal component of the electric displacement, and the direction of n has been taken into account. The *total* charge (fixed plus polarization) associated with the kth site is then $q_k^{tot} = q_k - (1 - 1/D_i)q_k = q_k/D_i$. In the limit as the charge radius R_c approaches zero (so that we realize the classical picture of point charges), the electric potential may be written:

$$\Phi(r) = \frac{1}{D_i} \sum_k \frac{q_k}{|r - r_k|} + \int_S \frac{\sigma(R) d^2R}{|r - R|}. \quad (4)$$

Our task now reduces to calculating the distribution of induced polarization charge $\sigma(R)$ on the solute-solvent boundary. Since a general analytic solution is not available for surfaces of arbitrary shape, we must resort to a numerical procedure.

Description of the Surface

Our computational approach involves an application of the method of surface boundary

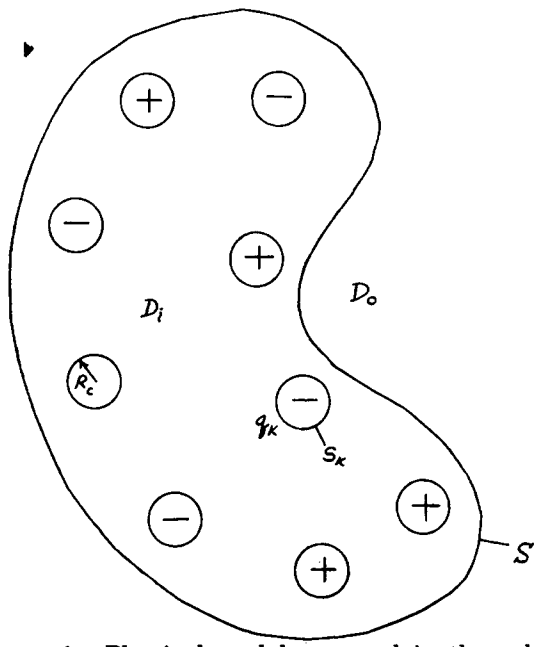

Figure 1. Physical model assumed in the calculations. The internal charges are initially assigned a finite radius R_c, which is eventually reduced to zero in our development. (The dielectric constant inside the spherical charges is irrelevant to our derivation, and is not assigned.)

elements.[17] The solute-solvent surface S is defined by a set of points (or *nodes*) with associated unit surface normals directed from the molecular interior toward the solvent. We assume that we are provided with a triangulation of the points, consisting of a set of connections (or *edges*) between nodes that serve to define a polyhedral surface with triangular faces (see Figure 2). Each face (or *element*) is then specified by a triple of interconnected nodes.

Given a set of triangulated nodes, we now define a smooth, piece-wise analytic description of the dielectric interface. As a first step, we replace the straight connections between nodes (which are implied by the initial triangulation) with curved arcs. Explicitly, we show that a pair of connected nodes, along with their unit normals, may be used to define a unique *cubic trajectory* in three-dimensional space. Let $\mathbf{x}(t)$ be this trajectory, parameterized by the dimensionless variable $t(0 \leq t \leq 1)$; then,

$$\mathbf{x}(t) = C_0 + C_1 t + C_2 t^2 + C_3 t^3 \qquad (5)$$

where $C_0, \ldots, C_3$ are vector constants to be determined. If the trajectory connects nodes i and j, with positions $\mathbf{x}_i$ and $\mathbf{x}_j$, we may immediately write

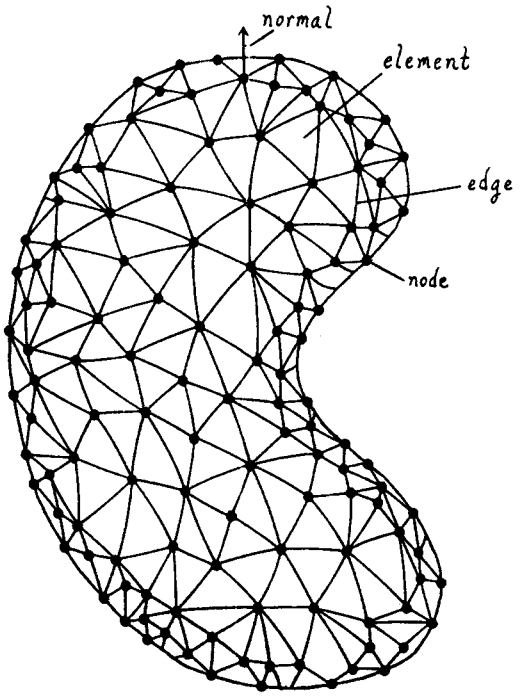

Figure 2. Triangulation of the molecular surface (dielectric interface). Unit normals point from the molecular interior toward the solvent.

$$\mathbf{x}(0) = \mathbf{x}_i = C_0$$
$$\mathbf{x}(1) = \mathbf{x}_j = C_0 + C_1 + C_2 + C_3 \qquad (6)$$

As a prelude to establishing a continuous normal on the interpolated surface, we will first define a normal along each trajectory between nodes (and in the process complete the specification of the constants $C_0, \ldots, C_3$). A normal to a smooth curve is naturally defined by the *curvature,* which is equal to the second derivative of the curve, provided that it is parameterized in terms of its arc length (given this condition, the curvature is always perpendicular to the tangent). While we have chosen to parameterize in terms of the dimensionless variable t (rather than the arc length), we may set the second derivative $d^2 \times /dt^2$ *parallel* to the normals at the endpoints. If the surface normals at nodes i and j are n_i and n_j respectively, this constraint leads to the equations

$$C_2 = \alpha n_i$$

and

$$C_3 = \frac{1}{3}(\beta n_j - \alpha n_i) \qquad (7)$$

where α and β are scalar constants to be determined. Finally, we set the tangent dx/dt perpendicular to the unit normals at the endpoints, which gives

$$C_1 \cdot n_i = 0$$

and

$$(C_1 + 2C_2 + 3C_3) \cdot n_j = 0\,. \qquad (8)$$

Simultaneous solution of equation sets 6–8 yields

$$\alpha = \frac{(\mathbf{x}_j - \mathbf{x}_i) \cdot [n_i(n_j \cdot n_j) + (1/2)n_j(n_i \cdot n_j)]}{(2/3)\,(n_i \cdot n_i)\,(n_j \cdot n_j) - (1/6)\,(n_i \cdot n_j)}$$

and

$$\beta = \frac{-(\mathbf{x}_j - \mathbf{x}_i) \cdot n_j - (1/3)\alpha(n_i \cdot n_j)}{(2/3)\,(n_j \cdot n_j)}\,. \qquad (9)$$

Given α and β, the vector constants $C_0, \ldots, C_3$ are uniquely defined by the expressions above. With the trajectory now completely determined, we can express the curvature $K(t)$ in terms of the second derivative $d^2\mathbf{x}/dt^2$, using the standard expression[18]

$$K(t) = \frac{1}{|d\mathbf{x}/dt|}\left[\frac{d^2\mathbf{x}}{dt^2} - \frac{\left\{\frac{d\mathbf{x}}{dt} \cdot \frac{d^2\mathbf{x}}{dt^2}\right\}}{|d\mathbf{x}/dt|^2}\frac{d\mathbf{x}}{dt}\right]. \qquad (10)$$

The unit normal to the trajectory is then given explicitly by

$$\mathrm{n}(t) = \mathrm{sign}(t)\frac{K(t)}{|K(t)|} \tag{11}$$

where $\mathrm{sign}(t) = \pm 1$, and is chosen so as to maintain a constant orientation of $\mathrm{n}(t)$ along the curve (if this factory were not included, the direction of $\mathrm{n}(t)$ would reverse at inflection points of the trajectory).

Now, as illustrated in Figure 3, we form a complete curvilinear element from three nodes (i, j and k) and their associated unit normals (n_i, n_j and n_k). We first construct two trajectories (two "sides") of the element, from node i to node j (trajectory x_{ij}), and from node i to node k (trajectory x_{ik}) The trajectories have associated unit normals n_{ij} and n_{ik}. The same variable u will parameterize both curves, so that a given value of u locates a point on each side.

Given $\mathrm{x}_{ij}(u)$, $\mathrm{x}_{ik}(u)$ and the normals $n_{ij}(u)$ and $n_{ik}(u)$, we can construct a "spanning trajectory" (Fig. 3) parameterized by a second variable v ($0 \le v \le 1$). In this way, any point on the curvilinear element is associated with a pair of local coordinates u and v. (When $u = 1$, the spanning trajectory forms the third side of the element.) By construction, the surface normal is continuous within the element, and in addition the normal along an edge is completely determined by the nodes at the endpoints. As a consequence, the interpolation scheme we have presented insures a smooth surface, with a normal that is continuous across element boundaries.

However, the surface, while smooth, is not analytic. That is, points are not located by

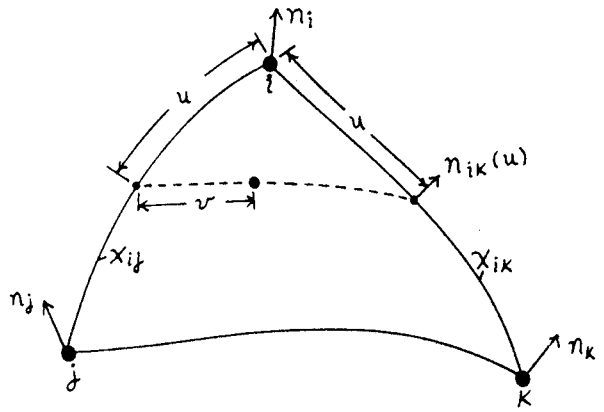

Figure 3. Formation of a curvilinear element. The two "base" trajectories (x_{ij} and x_{ik}) are determined completely by the node positions and normals; the "spanning" trajectory is defined by two points (and their associated normals) on the base trajectories.

an algebraic function of u and v, but by a constructive method. This means that the interpolation is not by itself appropriate for evaluating integrals over the surface (as will be required later in our development). To create a true piece-wise analytic surface, we proceed as follows. First, the mapping from the unit square ($0 \le u \le 1$, $0 \le v \le 1$)) to the curvilinear element is replaced by a mapping from the unit triangle, with local coordinates r and s (see Figure 4(a)). The change of coordinates is easily found to be

$$\left.\begin{aligned} u &= (r + s) \\ v &= s/(r + s) \end{aligned}\right\}(r + s) \neq 0$$
$$\left.\begin{aligned} u &= 0 \\ v &= 0 \end{aligned}\right\} r = s = 0 \tag{12}$$

We next use the constructive interpolation to map ten regularly-spaced points (Figure 4(b)) from the unit triangle to points $\{\mathrm{x}_k^{(j)}, k = 1, 10\}$ on the curvilinear element (here, the superscript indicates the jth element). Given the set of points $\{\mathrm{x}_k^{(j)}\}$, we can write an analytic expression for the element surface:

$$\mathrm{x}^{(j)}(r, s) = \sum_{k=1}^{10} \mathrm{N}_k(r, s)\mathrm{x}_k^{(j)}. \tag{13}$$

In Eq. (13), the $\mathrm{N}_k(r, s)$ are *Lagrangian interpolation polynomials* for a ten-point element. The method for deriving the polynomials is

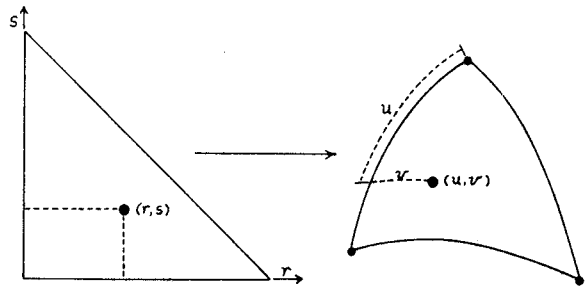

Figure 4.(a) Change of coordinates. Local coordinates (r, s) in the plane are mapped to curvilinear coordinates (u, v) in the surface element.

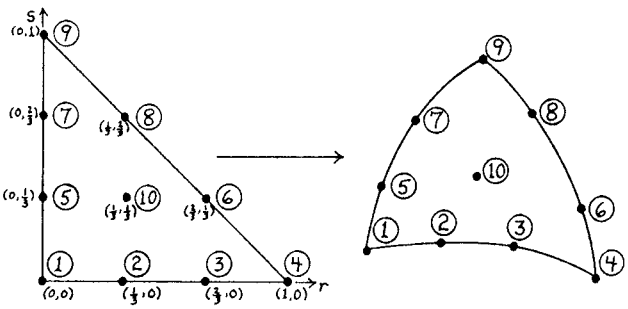

Figure 4.(b) Mapping of ten evenly-spaced points from the unit triangle to the curvilinear element.

presented in Zienkiewicz;[19] they are listed in Table I. We may now write the integral of some scalar field $F(r,s)$ defined on the element as follows:

$$\int_j F(r,s)dA = \int_0^1 dr \int_0^1 ds\ F(r,s)\omega^{(j)}(r,s) \tag{14}$$

where $\omega^{(j)}(r,s)$ is a "weight" associated with mapping an infinitesimal area $dA = drds$ from the unit triangle to the jth interpolated element. It is easily found to be

$$\omega^{(j)}(r,s) = \left| \frac{\partial \mathbf{x}^{(j)}(r,s)}{\partial r} \times \frac{\partial \mathbf{x}^{(j)}(r,s)}{\partial s} \right| \tag{15}$$

where we implicitly take the derivatives with respect to r and s of Eq. (13). In practice, the integral must be evaluated by numeric quadrature,

$$\int_j F(r,s)\ dA = \sum_l F(r_l,s_l)\omega^{(j)}(r_l,s_l)W_l \tag{16}$$

where the index l ranges over the quadrature points, and W_l is the weight associated with the lth point, which has local coordinates (r_l, s_l). (In the calculations that follow, integrations will be carried out using the Gauss-Radau quadrature rules for triangles.)[20]

Table I. Ten-Point Interpolation Functions.

$$N_1 = \frac{1}{2}L_1(3L_1 - 1)(3L_1 - 2)$$

$$N_2 = \frac{9}{2}L_1L_2(3L_1 - 1)$$

$$N_3 = \frac{9}{2}L_1L_2(3L_2 - 1)$$

$$N_4 = \frac{1}{2}L_2(3L_2 - 1)(3L_2 - 2)$$

$$N_5 = \frac{9}{2}L_1L_3(3L_1 - 1)$$

$$N_6 = \frac{9}{2}L_2L_3(3L_2 - 1)$$

$$N_7 = \frac{9}{2}L_1L_3(3L_3 - 1)$$

$$N_8 = \frac{9}{2}L_2L_3(3L_3 - 1)$$

$$N_9 = \frac{1}{2}L_3(3L_3 - 1)(3L_3 - 2)$$

$$N_{10} = 27L_1L_2L_3$$

where $L_1 = 1 - r - s$

$L_2 = r$

$L_3 = s$

Electrostatic Equations

In what follows, superscripts (in parentheses) will represent element indices, subscripts will indicate node indices.

We have shown previously[14] that the polarization-charge density at the ith node (σ_i) is related to the normal component of the electric field $(E \cdot n_i)$ at the node by

$$\sigma_i = \frac{1}{4\pi}\frac{D_i - D_o}{D_i} E \cdot n_i \tag{17}$$

The normal field $E \cdot n_i$ (which will be evaluated on the solvent side of the dielectric interface) has three components: 1) $E \cdot n_{(int)i}$, the contribution of the fixed, internal charges, 2) $E \cdot n_{(local)i}$, the contribution of the polarization charge in an infinitesimal region immediately around the node, and 3) $E \cdot n_{(surf)i}$, the contribution due to the rest of the surface (i.e. excluding the local region).

The contribution of the fixed charges is easily found using Coulomb's law,

$$E \cdot n_{(int)i} = \frac{1}{D_i}\sum_k q_k \frac{(\mathbf{x}_i - \mathbf{r}_k)\cdot n_i}{|\mathbf{x}_i - \mathbf{r}_k|^3} \tag{18}$$

where the subscript k ranges over the fixed charges, and the other symbols have been defined above. The local component, $E \cdot n_{(local)i}$ is found by a simple application of Gauss' law in the vicinity of the node:

$$E \cdot n_{(local)i} = 2\pi\sigma_i \tag{19}$$

To compute the contribution to the normal field arising from the remainder of the polarization-charge distribution, we must carry out a numeric integration over the surface. Explicitly,

$$E \cdot n_{(surf)i} = \sum_j \int_j \sigma^{(j)}(r,s) \cdot \frac{(\mathbf{x}_i - \mathbf{x}^{(j)}(r,s))\cdot n_i dA(r,s)}{|\mathbf{x}_i - \mathbf{x}^{(j)}(r,s)|^3} \tag{20}$$

where j ranges over all the elements, and $\sigma^{(j)}(r,s)$ is the distribution of surface polarization charge (as a function of local coordinates r and s) within the jth element. (The integrand of eq. (20) now corresponds to the general scalar field $F(r,s)$ of eq. (14). We note that while eq. (20) *formally* includes the local contribution to the normal field (eq. 19), the local contribution cannot be evaluated by con-

ventional numerical integration methods, and must be treated separately.

In order to evaluate the sum of integrals (20), it is necessary to find an expression $\sigma^{(j)}(r,s)$ for each element, and to relate these distributions to nodal polarization densities (since a set of calculated densities $\{\sigma_i\}$ is to be the final result of our computational technique). To accomplish this, we will assume linear interpolation (with respect to the local coordinates) of the induced surface density over each element. The jth element involves three nodes, which we will denote $1(j)$, $2(j)$ and $3(j)$. The distribution of polarization density is then given by

$$\sigma^{(j)}(r,s) = \sigma_{1(j)}(1 - r - s) + \sigma_{2(j)} r + \sigma_{3(j)} s \quad (21)$$

where the nodes $1(j)$, $2(j)$ and $3(j)$ are associated with respective local coordinates $(0,0)$, $(1,0)$ and $(0,1)$ in the r-s plane. Eq. (20) may now be rewritten

$$E \cdot n_{(surf)i} = \sum_j [\mathrm{K}^{(j)}_{i,1(j)} \sigma_{1(j)} + \mathrm{K}^{(j)}_{i,2(j)} \sigma_{2(j)} + \mathrm{K}^{(j)}_{i,3(j)} \sigma_{3(j)}] \quad (22)$$

where the K-coefficients are defined by

$$\mathrm{K}^{(j)}_{i,1(j)} = \int_j \frac{(\mathbf{x}_i - \mathbf{x}^{(j)}(r,s)) \cdot n_i}{|\mathbf{x}_i - \mathbf{x}^{(j)}(r,s)|^3} (1 - r - s)\, dA(r,s),$$

$$\mathrm{K}^{(j)}_{i,2(j)} = \int_j \frac{(\mathbf{x}_i - \mathbf{x}^{(j)}(r,s)) \cdot n_i}{|\mathbf{x}_i - \mathbf{x}^{(j)}(r,s)|^3} r\, dA(r,s), \quad (23)$$

and

$$\mathrm{K}^{(j)}_{i,3(j)} = \int_j \frac{(\mathbf{x}_i - \mathbf{x}^{(j)}(r,s)) \cdot n_i}{|\mathbf{x}_i - \mathbf{x}^{(j)}(r,s)|^3} s\, dA(r,s).$$

Assume that N_n nodes are used to define the surface, along with N_e elements, and let the nodal polarization densities be arranged as a column vector $[\sigma]$. Similarly, the values of $E \cdot n_{(surf)i}$ are placed in a column vector $[E \cdot n_{(surf)}]$. Eq. (22) can then be written in matrix form as follows:

$$[E \cdot n_{(surf)}] = \sum_j [\mathrm{K}^{(j)}][\sigma] \quad (24)$$

where $[\mathrm{K}^{(j)}]$ is an $N_n \times N_n$ matrix defined by

$$\mathrm{K}_{lm} = \begin{cases} \mathrm{K}^{(j)}_{i,1(j)} & l = i,\ m = 1(j) \\ \mathrm{K}^{(j)}_{i,2(j)} & l = i,\ m = 2(j) \\ \mathrm{K}^{(j)}_{i,3(j)} & l = i,\ m = 3(j) \end{cases} \quad (25)$$

Next, we define

$$[K] = \sum_j [K^{(j)}] \quad (26)$$

(The process of *equation assembly* represented by eq. (26) is well-described in ref. (19). The matrix expression for the total normal electric field may now be written,

$$[E \cdot n] = 2\pi[\sigma] + [\mathrm{K}][\sigma] + [E \cdot n_{(int)}] \quad (27)$$

where the entries for the vector $[E \cdot n_{(int)}]$ are given by eq. (18). We also recast eq. (17) (our original expression for σ_i) in matrix form:

$$[\sigma] = \frac{D_i - D_o}{4\pi S_i} [E \cdot n]. \quad (28)$$

Substituting eq. (27) into eq. (28) and rearranging, we achieve our final result,

$$\{[\mathrm{I}] - f[\mathrm{K}]\}[\sigma] = f[E \cdot n_{(int)}] \quad (29)$$

where [I] is the unit matrix, and the scalar f is given by

$$f = \frac{1}{2\pi} \frac{D_i - D_o}{D_i + D_o}. \quad (30)$$

The *system matrix* $\{[\mathrm{I}] - f[\mathrm{K}]\}$ depends only on the geometry of the dielectric interface, and the triangulation chosen to model it. The right-hand side of eq. (29) depends only on the locations and sizes of the fixed internal charges.

Eq. (29) embodies a system of simultaneous linear equations, which may be solved to yield the nodal polarization densities. Given $[\sigma]$ and the interpolation of the dielectric interface, the potential at any point r is easily found by applying eq. (4).

Triangulation

While the derivation we have presented is more complicated than our previous development,[14] application is reasonably straightforward *once the dielectric interface has been triangulated.* This is in fact the *central* problem associated with the method. In a 1985 paper, Connolly[21] describes an algorithm for triangulating the solvent-accessible surfaces of molecules, given a list of atomic coordinates and a set of atomic radii. The method could, in principle, be used to prepare triangulations (or *meshes*) for electrostatic calculations. Unfortunately, the associated computer programs were unavailable, and we have instead relied on our own algorithm.

We begin with a set of nodes on the surface, generated by any convenient means. For calculations of the molecular electric potential, we will employ a dot surface (of the kind widely used for computer graphic displays) generated by Connolly's computer program,[22] which covers the molecular solvent-accessible surface with a fairly uniform distribution of points (nodes). Our algorithm begins by connecting node #1 and two of its neighbors, selected to form a triangle of the smallest possible perimeter. The three connections thus formed will be termed *free edges,* since they are part of only one element, and therefore lie on the boundary of the developing triangulation. Given a collection of nodes and an initial set of edges (which in the general case may not all be free edges), the algorithm proceeds as follows:

1) The list of edges is scanned for the first free edge (say, the kth). If no free edge is found (i.e. all the edges are part of two different elements), the algorithm is finished.
2) Suppose the kth edge connects nodes k_1 and k_2. Our goal is to create a new element by connecting k_1 and k_2 to some node m. First, from the set of all nodes, we select a subset from which m may be chosen. (The criteria involved in selecting the subset will be discussed below.)
3) From the subset selected in step 2, we choose the node m which forms the triangle k_1-k_2-m of smallest possible perimeter.
4) If edge k_1-m does not already exist, it is added to the list of edges, and similarly for k_2-m. In many instances, the new connections will be free edges (that is, only associated with the new element k_1-k_2-m). However, in regions where the triangulation closes upon itself (Figure 5), one or both edges may be involved in two elements; while such connections will be added to the list of edges, they will not be labeled as "free" edges.

Steps 1 through 4 are repeated until the list of free edges is exhausted.

The most critical step in the algorithm is the selection of the subset from which m is chosen. Three criteria are applied. First, all

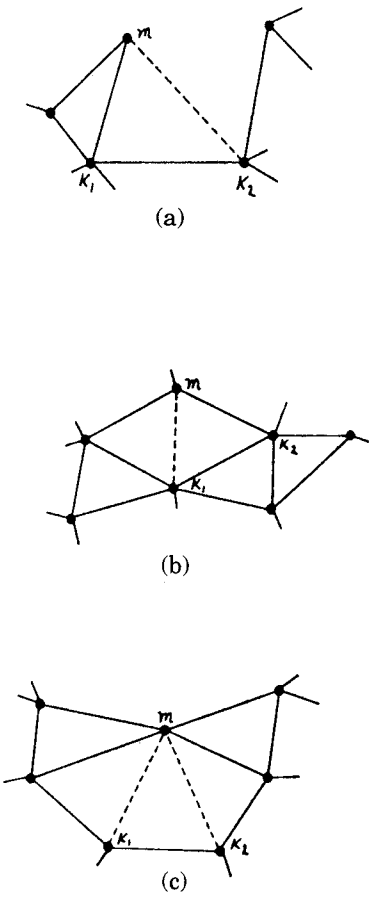

Figure 5. Closure of the mesh upon itself. The free edge is $k_1 - k_2$, m is the node chosen for connection into a new element. Newly-added edges are indicated by dashed lines. The diagram shows the creation of (a) one new edge and one new element, (b) one new edge and two new elements, and (c) two new edges and three new elements.

nodes that lie outside a cut-off distance (which is selected beforehand) from either k_1 or k_2 are eliminated from consideration. Secondly, all nodes included in the subset must lie on the side of edge k_1-k_2 that is opposite to k_3, the remaining node in the element that includes edge k_1-k_2. The final criterion is that neither of the generated edges (k_1-m or k_2-m) may intersect a previously-defined element. This possibility is illustrated in Figure 6(a), where we see the free edge under consideration, along with two potential connections. It is apparent that formation of element k_1-k_2-m_1 would result in just such an intersection (with previously-defined element k_1-m_1-m_2). To avoid such occurrences, the following test is applied: Referring to Figure 6(b), for each m under consideration, we construct a line from the midpoint p of edge k_1-k_2 to m. Next, we take each element in turn that includes m in its definition,

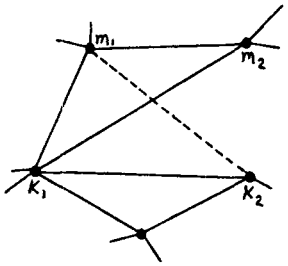

Figure 6. Illustration of edge-element intersection. (a) The formation of element $k_1 - k_2 - m_1$ will result in an intersection of a new edge with a previously-defined element. Formation of $k_1 - k_2 - m_1$ would not result in an intersection.

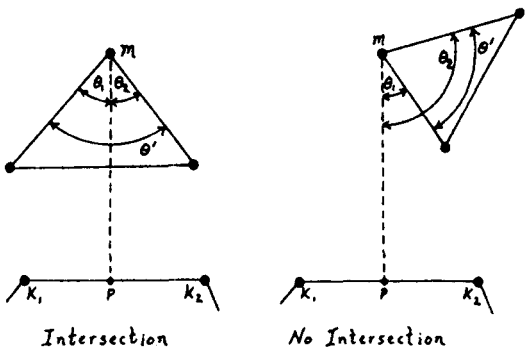

Figure 6.(b) (Left): Formation of element $k_1 - k_2 - m_1$ will result in an intersection; in this case, the sum of the angles Θ_1 and Θ_2 formed by segment $p - m$ equals the angle Θ' defined in the figure. (Right): if $(\Theta_1 + \Theta_2) > \Theta'$, we assume that no intersection will occur. In the figure, $p - m$ is assumed to be projected onto the plane defined by the three nodes of the element which includes m.

project the line p-m onto the plane of the element, and compute the angles θ_1, θ_2 and θ' shown in the figure. It is easy to see that the projection of p-m will intersect the element if and only if $\theta_1 + \theta_2 = \theta'$. If this is the case for any of the elements that involve m, then the node will not be included in the subset of possible connections. While this test does not test separately for intersections by k_1-m and k_2-m, it has been found adequate in practice.

The algorithm described above has been used (with partial success) to prepare triangulations for a number of small molecules and test systems. The integrity of a triangulation is easily tested by computing the Euler characteristic[23] (E_c) of the resulting mesh,

$$E_c = N_n + N_e - N_c \qquad (31)$$

where N_n is the number of nodes, N_e is the number of elements, and N_c is the number of connections (edges). E_c must always equal two for a properly triangulated system. If E_c is not equal to two, then the mesh either has "holes" (faces with more than three sides), or includes extraneous edges that cut across element boundaries.

It should be noted that the algorithm we have described is only successful if the distribution of nodes is not too irregular. In general, as the surface being modeled becomes more complex and convoluted, a higher density of points is required to insure a proper triangulation. In the event that the algorithm is unsuccessful, "illegal" edges (i.e. edges that are not part of exactly two elements) may be located and removed with the aid of an interactive graphics program, which provides the facility to easily rearrange connections between nodes.

III. APPLICATIONS

A set of FORTRAN computer programs has been prepared to produce a triangulated smooth surface from a set of nodes, build a system matrix (given the internal and external dielectric constants), and solve the resulting set of equations for a specified configuration of fixed charges. The resulting array of nodal polarization-charge densities may then be used by auxiliary programs to find the electric potential at selected positions, compute electrostatic forces at charged sites, calculate interaction energies, etc. The authors will provide copies of the programs upon request.

Comparison with an Analytic Solution

In order to test the reliability and accuracy of the method, it is necessary to compute the electric potential of a system for which an analytic solution is available. We choose to calculate the potential of a sphere of 15 Å radius (about the size of a small protein), for two charge positions: at radius 5 and 13.5 Å. The charge is taken as unit negative, with an effective radius (i.e. distance of closest approach to the dielectric interface) of 1.5 Å, thus suggesting an ionized carboxyl group. We set $D_i = 1$, $D_o = 78$.

Figure 7 shows the triangulation of the spherical interface employed in the calculations. The axis along which the charge is placed is perpendicular to the plane of the diagram. The mesh has three regions (all apparent in the figure), corresponding to a high, low or intermediate density of nodes. The charge placements are closest to the high-density domain, so that the greatest concentration of elements will be found in

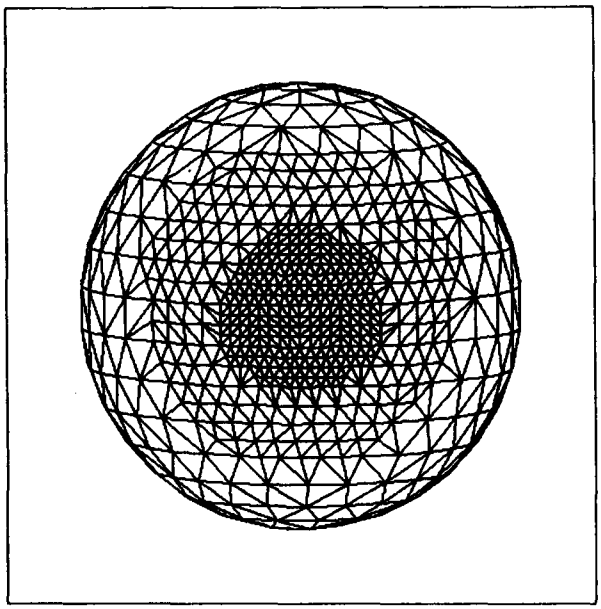

Figure 7. Triangulation of the spherical interface. Fixed charges are placed along an axis that passes through the center of the sphere, and approximately through the center of the region of highest node density.

the region where the polarization density changes most rapidly. The dielectric interface is modeled with a total of 704 nodes and 1404 elements. (To create the mesh shown in Figure 7, a process of subdivision was applied to an initial triangulation of a uniformly-distributed set of nodes. Two rounds of subdivision were used to produce the three regions illustrated.)

The results for the interior of the spherical interface are shown in Figure 8. Equipotentials (in a cross-section through the center of the spherical interface) are plotted in units of Kcal/mol for a unit positive test charge, and for both placements of the fixed source charge. Solid contours show the results of the polarization-charge calculation, dashed contours represent the analytic (i.e. exact) solution. It is clear that in the interior there is excellent agreement between the results of the polarization-charge model and the exact solution of the electric potential. In Figure 9, the error associated with the polarization-charge results (for both charge placements) is illustrated by equicontours of percentage error. It is seen that the error is never worse than 3%, and is generally much better (especially near the charge). As an additional test, we calculate the total amount of polarization charge on the surface. A simple application of Gauss' law yields the *exact* value

$$q_{\text{pol(exct)}} = q_{in}\left[\frac{1}{D_o} - \frac{1}{D_i}\right] \tag{32}$$

where q_{in} is the total fixed charge inside the dielectric interface. For our system ($D_i = 1$, $D_o = 78, q_{in} = -1$) we find $q_{\text{pol(exct)}} = +0.9872$; the *computed* values (found by numerical integration over the surface) are 0.9890 and 0.9874, corresponding to the two charge placements (at 5 and 13.5 Å, respectively). The errors associated with the computed values are 0.18% and 0.02%, again showing excellent agreement between the results of the polarization-charge technique and analytic predictions.

We now turn out attention to the electric potential *outside* the dielectric interface. In Figure 10(a), we see a set of equipotential contours computed in the solvent surrounding the spherical interface, for the charge at 13.5 Å radius (this is the only placement for which we expect a potential of significant magnitude to exist in the solvent). In contrast to the results for the interior, we now find a less satisfactory agreement between the predictions of the polarization-charge model and the analytic solution. Contours of percentage error for the external potential are shown in Figure 10(b), and it is seen that the error is now 20% in the vicinity of the fixed charge. Given that one of our primary goals is to calculate the interaction of molecules separated by solvent, the inability to accurately determine the potential outside the dielectric interface poses a serious problem. The source of this difficulty, and its solution, are discussed in the next section.

The Exterior Potential

Suppose we allow the external dielectric constant to approach infinity. Then the scalar $f \rightarrow f_o = -1/2\pi$, and we find the solution $[\sigma_o]$ appropriate for a cavity (of dielectric constant D_i) embedded in a *conducting* continuum:

$$\{[\mathrm{I}] - f_o[K]\}[\sigma_o] = f_o[E \cdot n_{(\text{int})}]. \tag{33}$$

The electric field in a conductor vanishes; therefore, the external potential is identically zero. We may rewrite Eq. (4) for the potential Φ_o found in the conducting case:

$$\Phi_o(r_o) = \frac{1}{D_i}\sum_k \frac{q_k}{|r_o - r_k|} + \int_S \frac{\sigma_o(R)\, d^2R}{|r_o - R|} = 0 \tag{34}$$

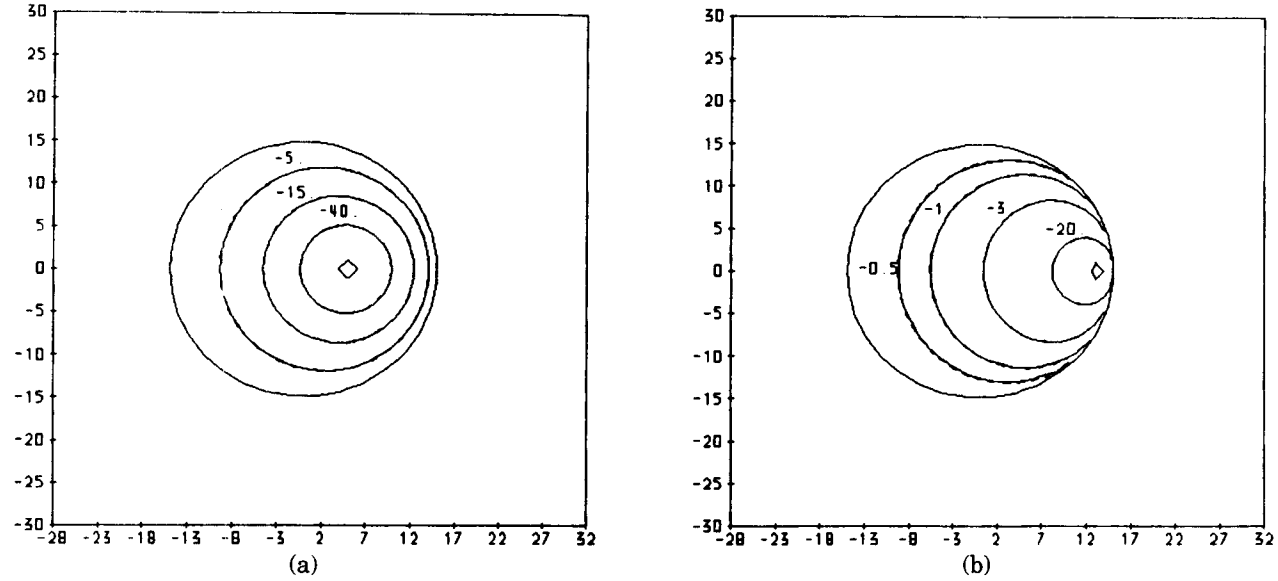

Figure 8. Equipotentials for charge placements at (a) 5 Å and (b) 13.5 Å radius. Contours are plotted in a cross-section through the center of the sphere; the section also passes through the position of the fixed charge, which is indicated in each diagram. Distance in Å is measured along the borders of the diagram.

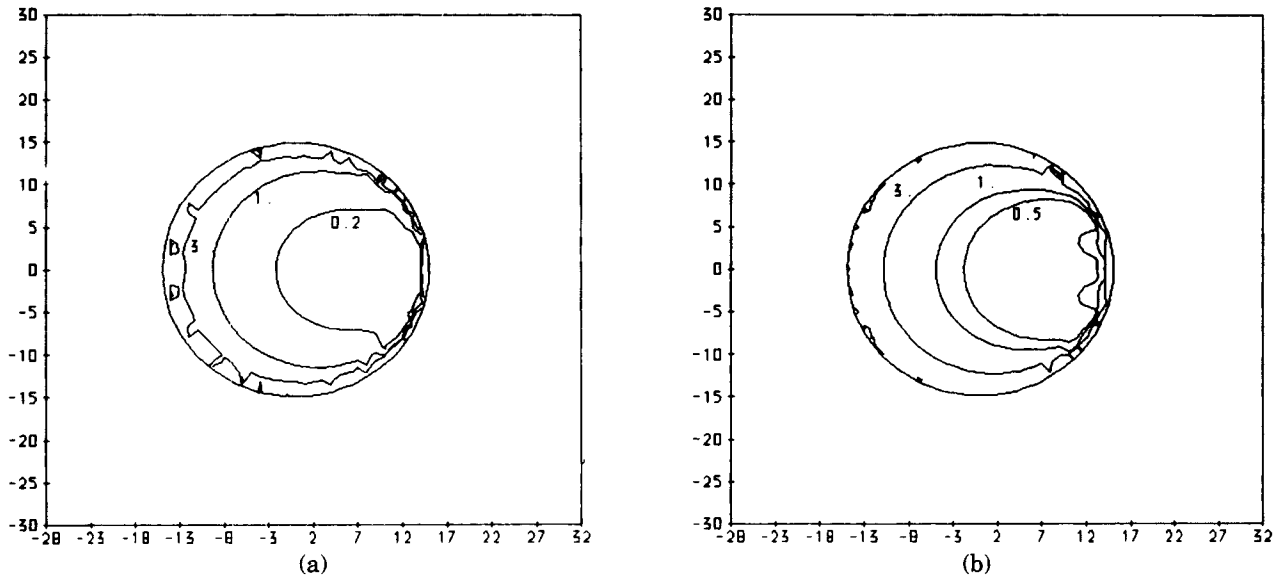

Figure 9. Contours of percentage error (with respect to the analytic solution) for the polarization charge results. The figures (a) and (b) correspond to charge placements at 5 Å and 13.5 Å radius, respectively.

for points r_o outside the dielectric interface. (Here, $\sigma_o(R)$ is the theoretical exact solution on the interface.) Let $\delta f = f - f_o$, so that the change in the system matrix in moving to finite D_o is $-\delta f$[K].

We expect δf to be small compared to f_o, assuming that D_i is small compared to D_o (for our system, $f_o = -0.159$, $\delta f = +0.004$). As a consequence, the solution for finite D_o, $[\sigma]$, will be nearly the same as the conducting solution, $[\sigma_o]$. We define the difference by

$$[\sigma] = [\sigma_o] + [\delta\sigma] \tag{35}$$

or $\sigma(R) = \sigma_o(R) + \delta\sigma(R)$, in terms of the theoretical (exact) solutions over the surface S. Referring to eq. (34), we may now write the external potential Φ_{ext} for *finite* D_o as

$$\Phi_{ext}(r_o) = \int_S \frac{\delta\sigma(R)\, d^2\mathrm{R}}{|r_o - \mathrm{R}|}. \tag{36}$$

(Note that the internal charges, $\{q_k\}$, do not enter directly into eq. (36). The difficulty encountered in computing the potential outside the dielectric interface is now clear; any error in the calculated distribution of polarization

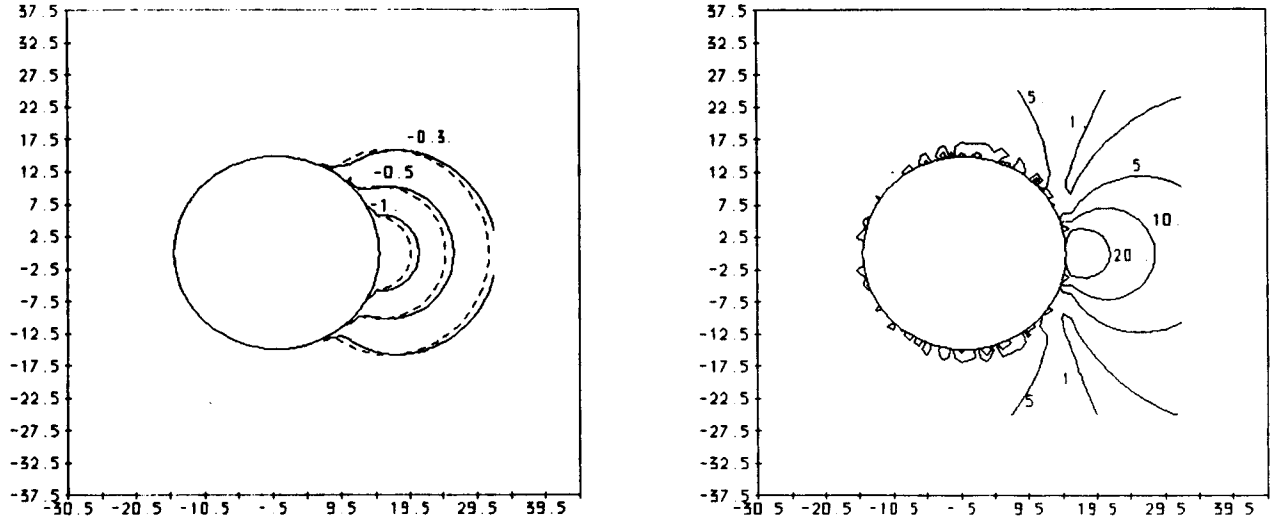

(a) (b)

Figure 10. The external potential for charge placement at 13.5 Å radius. (a) Equipotentials in a cross-section through the center of the sphere; (b) Contours of percentage error (with respect to the analytic solution).

charge (whether due to errors in the σ_i's, or the unavoidable error associated with linear interpolation) may be of the same order as $\delta\sigma$, making an accurate calculation of Φ_{ext} impossible.

Fortunately, it is possible to develop an alternative formulation in which the vector $[\delta\sigma]$ is computed *directly*. Substituting eq. (35) into eq. (29) yields

$$\{[I] - f[\mathrm{K}]\}([\sigma_o] + [\delta\sigma]) = f[E \cdot n_{(\mathrm{int})}]. \tag{37}$$

Solving eq. (33) and (37) simultaneously, we find

$$\{[I] - f[K]\}[\delta\sigma] = \frac{f - f_o}{f_o}[\sigma_o]. \tag{38}$$

So, given an estimate of the solution for the conducting case, we can easily solve for $[\delta\sigma]$; furthermore, we expect the solutions $[\delta\sigma]$ and $[\sigma]$ to be of comparable accuracy. In practice, there are two methods for finding $[\delta\sigma]$—either by solving eq. (38) (given $[\sigma_o]$), or by finding $[\sigma]$ and $[\sigma_o]$ separately, and subtracting ($[\delta\sigma] = [\sigma] - [\sigma_o]$). It is easy to verify that $[\delta\sigma]$ found by the second method will also satisfy eq. (38).[24]

The results of the preceding analysis for the spherical interface are shown in Figure 11(a). Here, exterior equipotentials (computed from $[\delta\sigma]$) are plotted for the charge placement at 13.5 Å radius. We now find excellent agreement between the results of the polarization-charge method and the analytic solution (see Figure 11(b)). In addition, for the conducting case, it is easy to plot computed and analytic profiles of $\sigma_o(R)$ as a function of angle for a plane passing through the sphere (see Figure 12(a)), and it is seen that the analytic function is well-reproduced by our numerical technique for the charge placement near the surface. In Figure 12(b), we show $\delta\sigma(R)$ (computed by the polarization-charge method), and include the analytic $\sigma_o(R)$ for comparison. As expected, the size of $\delta\sigma(R)$ is very small compared to $\sigma_o(R)$.

Calculations for Biomolecules

We now present electrostatic calculations for three molecules of biological interest: the neurotransmitter serotonin[25] (in both neutral and cationic forms), thyrotropin-releasing hormone[26] (cationic form), and the neutral cyclic hexapeptide, PG3 ((-Pro-Gly)$_3$), a calcium-binding molecule.[27,28] For systems of arbitrary shape, the results of the polarization-charge technique cannot be compared with an analytic solution; therefore, as a test of accuracy, the calculations are carried out *twice*, with a significantly higher density of nodes in the second calculation. If the results of the second calculation (which is presumably the most accurate) do not differ dramatically from the first, then we are assured that the high-density solution is of reasonable accuracy (i.e. the computed potential has *converged*, in the finite-element sense).[19]

In Table II, we summarize the characteristics of the meshes employed in the calcu-

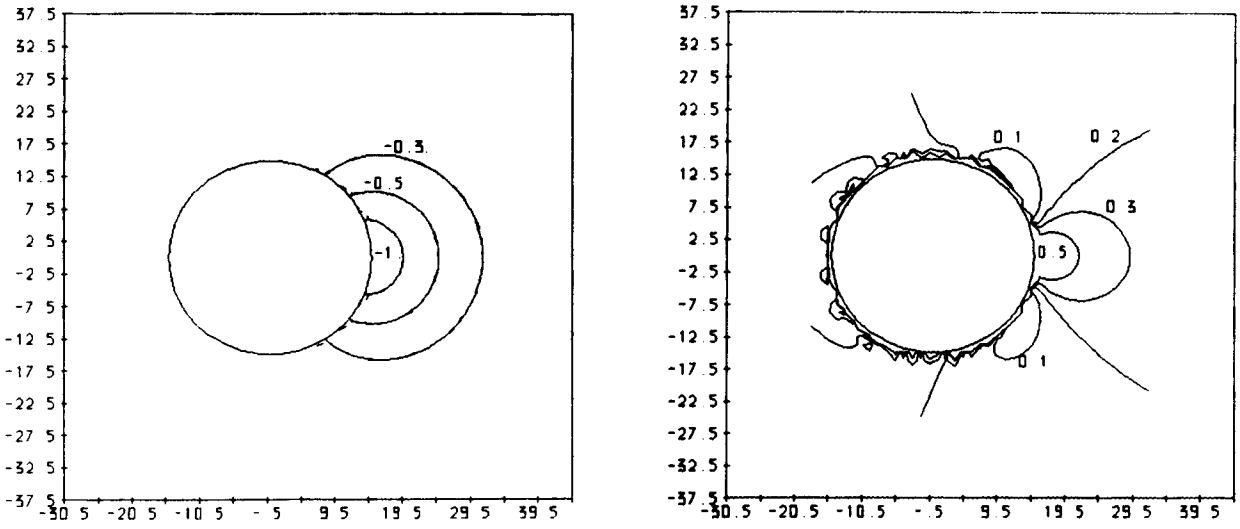

(a) (b)

Figure 11. A repetition of Fig. 10, with the external potential computed using the distribution $\delta\sigma$.

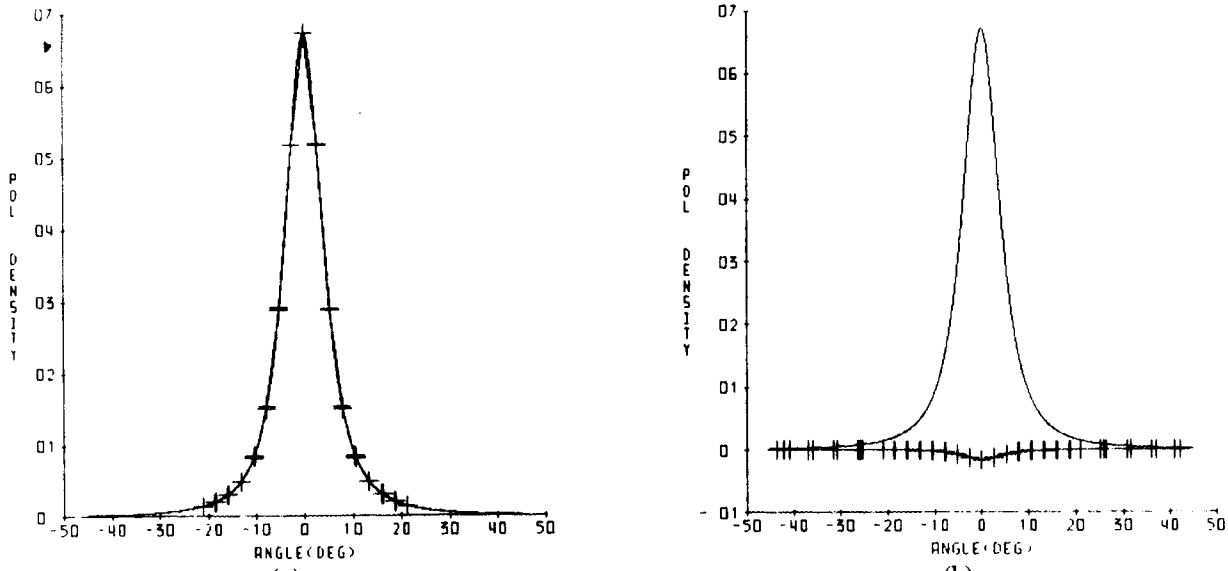

(a) (b)

Figure 12. Profiles of polarization-charge vs. angle for a cross-section through the spherical interface. The angle is measured from the axis on which the charge is placed. (a) Comparison of analytic (dashed) and polarization-charge results (solid) for the conducting solution. The cross-marks indicate where element edges pass through the plane of the section. (b) Comparison of the exact conducting solution (top curve), and the computed distribution $\delta\sigma$ (bottom curve).

Table II. Results for Biomolecules.

Molecule	# nodes	# elems	qpol exact	qpol comp	Node Density	ΔW(kcal/mol)	Time
Serotonin(neu)	382	760	0	−0.0005	1.73/Å^2	−4.885	16 min
Serotonin(neu)	698	1388	0	+0.0045	3.15/Å^2	−5.016	—
Serotonin(cat)	374	744	−.9872	−.9933	1.69/Å^2	−58.223	16 min
Serotonin(cat)	860	1716	−.9872	−.9917	3.89/Å^2	−58.345	1 hr 46 min
TRH*	328	652	−.9872	−.9816	1.12/Å^2	−48.354	12 min
TRH	694	1384	−.9872	−.9907	1.89/Å^2	−48.934	—
PG3	1083	2162	0	0.0108	2.40/Å^2	−16.874	—
PG3	1449	2894	0	0.0038	3.20/Å^2	−16.368	5 hr 10 min

*Thyrotropin-Releasing Hormone.
All times for a VAX 11/785.

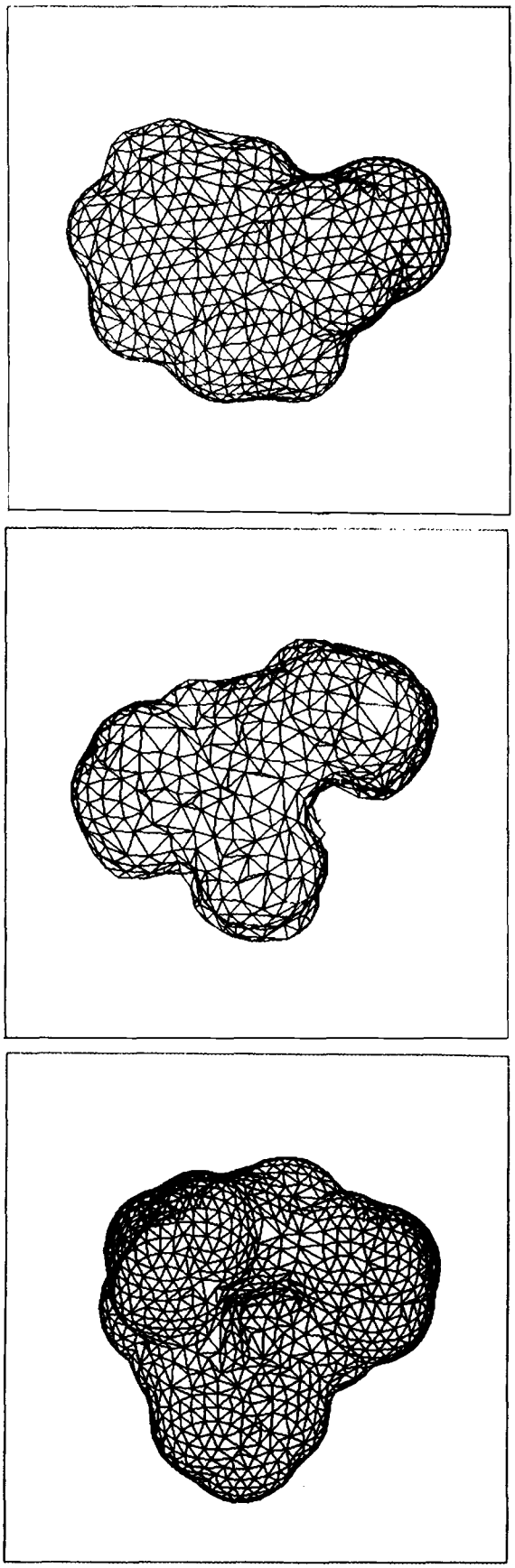

Figure 13. Meshes for electrostatic calculations, for serotonin cation (a), thyrotropin-releasing hormone cation (b), and the hexapeptide PG3 (c). We have shown only the "high-density" mesh generated for each molecule. The "pocket" apparent in (c) corresponds to the calcium-binding site. (Note that only the cationic form of serotonin is shown.)

lations. The number of nodes used to model each molecular surface can be selected (approximately) by adjusting the density parameter submitted to Connolly's dot-surface program (the densities quoted in the table are then found by dividing the number of nodes by an accurate estimate of the molecular surface area). The radii of the various atom types are set equal to the cavity radii developed in ref. 29 for computations of the hydration enthalpy of organic ions. Triangulations were carried out using the algorithm described above; graphic depictions of some of the resulting meshes are presented in Figure 13.

The molecular charge distributions were approximated by atom–centered charges as follows: For serotonin, 6-31G charges were used for the neutral form, STO-3G charges for the cation. CNDO charges were used for thyrotropin-releasing hormone. The partial charges for PG3 were taken from the CHARMM[30] molecular mechanics program.

For each mesh (and associated set of internal charges), electrostatic calculations were carried out as described above, to find both $[\sigma]$ and $[\delta\sigma]$. The external dielectric constant was taken as 78, the internal constant was set to 1 (since all polarization effects are implicitly included in the quantum calculations that generated the charge distributions). In Table II, we report the computed energy of stabilization ΔW of the internal charges by the total distribution of induced polarization charge, for each of the molecules considered (and for both the high- and low-accuracy solutions). ΔW approximates the hydration enthalpy for a charged specie. We also list the computed net polarization charge ($q_{\text{pol(comp)}}$), and the theoretical exact value ($q_{\text{pol(exct)}}$) for each of the calculations, along with some representative computing times (for construction of the system matrix, plus solution of the resulting system of equations).

In Figure 14, we present equipotential contours (arising from the distribution $[\delta\sigma]$) for the three molecules considered (including the neutral and charged forms of serotonin). In each case, solid contours are associated with the high accuracy solution, broken contours with the low-accuracy solution. It is seen that the convergence of the computed potentials is excellent on the whole, and inspection of Table II reveals that the hydration energy ΔW is also stable with respect to increases in node density. Convergence is more rapid for the cations than for neutral serotonin

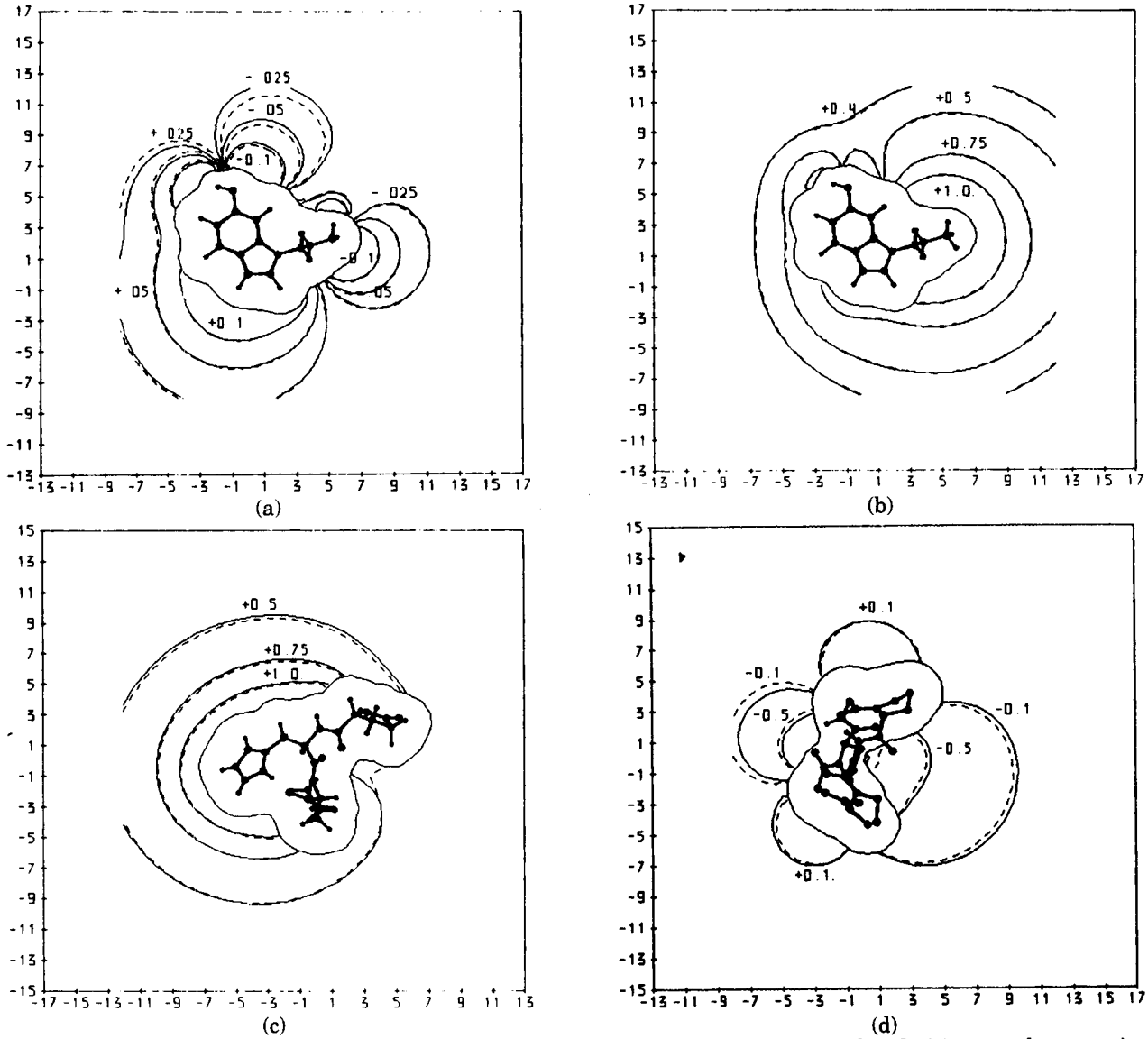

Figure 14. Equipotential contours in cross-sections through the molecules considered: (a) neutral serotonin, (b) serotonin cation, (c) thyrotropin-releasing hormone (TRH), and (d) PG3. In each case, the high accuracy solution is shown with solid contours, the low-accuracy solution is dashed. In each figure, the *complete* molecule is shown, along with the *intersection* of the dielectric interface and the plane of the cross-section (this is why part of PG3 appears to lie outside the dielectric boundary). Inspection of the meshes for TRH suggests that the deviation of the high- and low-accuracy solutions in one region near the surface may arise from locally inadequate modeling of the interface in the low-accuracy case. The region of negative potential on the right-hand side of the PG3 cross-section is near the calcium-binding site. Again, distance in Å is measured along the border of each diagram.

and PG3 (also a neutral molecule), where the computed contours change noticeably (although not dramatically) with an increase in node density. It should be noted, however, that for neutral serotonin the potential computed in the solvent is of very small magnitude; in fact, none of the contours displayed is of physiological significance (i.e. greater than ≈0.5 kcal/mol). In the case of PG3, the potential in the solvent is also of small magnitude, but here the partial alignment of peptide dipoles creates a region of significant potential in the vicinity of the calcium-binding site.

Several features of the computed potentials should be noted. First, for both cations, potentials of thermodynamic significance are seen to extend 6 to 8 Å into the solvent, effectively expanding the region over which the molecule may have physical effects. (In the case of the cationic form of serotonin, strong positive potential is largely confined to the vicinity of the amino side-chain, supporting the contention of Weinstein et al.[31] that the polar side-

chain plays an important role in "leading" the transmitter into its receptor). The neutral molecules, while they contain partial charges of significant magnitude, have their electrostatic effects largely damped by the polarization of the solvent. Specifically our results would indicate that the neutral form of serotonin will interact with other molecules only at very short range. As noted above, while the potential of PG3 does not extend far into the solvent, a localized region of thermodynamically-significant negative potential is observed at the calcium-binding site. (Fig. 14d)

IV. DISCUSSION

In our previous article, we described our general approach (that is, the consideration of induced polarization charge, and the modeling of dielectric interfaces by surface elements) as a "finite–element" technique. It has since been pointed out (see ref. 29) that our approach belongs in the class of *boundary element methods,*[17] which have been used in engineering to solve a variety of potential problems, including electrostatics. Also, an early application of polarization-charge methods to quantum chemistry is found in a paper by Miertus et al.,[32] although their methodology does not include true surface elements, or the matrix formalism we have adopted. In a recent article, Constanciel[33] has introduced electrostatics into theoretical quantum-chemical calculations, using a derivation similar in spirit to our previous development.[14] Working along different lines, Shaw[34] has advanced an *analytic* theory based on polarization-charge concepts, which holds promise for the computation of electrostatic interactions in biomolecules.

The polarization-charge approach enjoys a number of advantages over the finite-difference method. Most importantly, the use of two-dimensional surface elements provides a significant reduction in computing time (for a given level of accuracy), and permits very detailed modeling of the dielectric interface (this is critical if we are to consider ionized sites that lie near the molecular surface). In addition, since the geometry of the dielectric boundary is represented by the coefficient matrix of a system of simultaneous equations, standard techniques are available that allow $[\sigma]$ to be rapidly recomputed for new distributions of internal charge; this may be of special importance for studies of titration behavior. A further practical benefit of the method is its *flexibility.* As an example, in the test calculation for the spherical interface, it was an easy matter to subdivide the mesh in regions where the polarization density changed most rapidly, effectively allowing the bulk of the computation time to be devoted to the most critical part of the physical system. Analogous techniques are not available for finite-difference calculations of the molecular potential. As an additional example, the polarization-charge technique permits wide lattitude in the method chosen to model the *molecular interior.* In particular, it is possible to use either discrete or continuous fixed charge distributions, and to specify individual polarizable sites in the molecular interior (this may be important for proteins, which possess a complicated internal structure). While such complexities are not incorporated into the calculations presented here, they represent a straightforward extension of the model. In contrast, the resolution presently attainable with the finite-difference technique does not admit the detailed analysis of the effects of the internal structure of molecules.

It is important to consider the node densities that are required to achieve convergence of the electric potential. The somewhat limited evidence presented in Table II would suggest that a density of 1–2 nodes/Å^2 is sufficient for convergence in the case of charged molecules, while a density of 2–4 nodes/Å^2 is required for neutral species. (The density of nodes in the high-density region of our spherical interface is found to be approximately 2 nodes/Å^2.) While we have had reasonable success in achieving convergence for small molecules, our ultimate goal is to accurately calculate the electrostatic potential of proteins, given the physical assumptions we have adopted. To achieve the node densities described above (and, presumably, the same level of accuracy) will require that 5,000–10,000 nodes be used to model the surface of a medium-size protein. This presents a formidable computational task, but one that is easily accessible on modern computers. An additional challenge is posed by the problem of triangulating the surfaces of proteins, which are considerably more complicated than those of the small molecules treated here. In particular, it will be necessary to de-

termine what density of nodes is required for the surface interpolation scheme we have presented to accurately follow the protein solvent-accessible surface. At present, efforts are directed toward improving the methods used to define and triangulate the protein surface, so that the computational methods we have described may become practical for macromolecules.

The authors are indebted to Dr. Peter B. Shaw (Penn State University Physics Department) for his careful reading of the manuscript, and for many helpful discussions. One of us (R.J.Z.) would like to thank Dr. Harel Weinstein for useful and stimulating discussions. We would like to thank Dr. Kenji Hori for providing coordinates for PG3, as well as a molecular graphics routine. Thanks also to Richard Lanzara for supplying partial charges and coordinates for thyrotropin-releasing hormone. This work was supported in part by National Institute on Drug Abuse Grant DA-01875, National Science Foundation Grant BNS83-03373, US Environmental Protection Agency Grant CR811006, and National Science Foundation Grant DMB-8519273. We are indebted to Dr. Michael Liebman (Mount Sinai) for providing access to computing facilities under a grant from ImClone Systems, Inc.

References

1. P.A. Kollman and D.M. Hayes, *J. Am. Chem. Soc.*, **98**, 3335–3345, (1976).
2. E.D. Getzoff, J.A. Tainer, P.K. Weiner, P.A. Kollman, J.S. Richardson and J.C. Richardson, *Nature*, **306**, 287–290, (1983).
3. I. Klapper, R. Hagstrom, R. Fine, K. Sharp and B. Honig, *Proteins: Structure, Function and Genetics*, **1**, 47–59, (1986).
4. W.H. Orttung, *Biochemistry*, **9**, 2394–2402, (1970).
5. C. Tanford and R. Roxby, *Biochemistry*, **11**, 2192–2198, (1972).
6. J.B. Matthew, *Ann. Rev. Biophys. Biophys. Chem.*, **14**, 387–417, (1985).
7. J.A. McCammon and M. Karplus, *Ann. Rev. Phys. Chem.*, **31**, 29–45, (1980).
8. C.F. Wong and J.A. McCammon, *J. Am. Chem. Soc.*, **108**, 3830–3832, (1986).
9. M. Mezei, P.K. Mehrotra and D.L. Beveridge, *J. Am. Chem. Soc.*, **107**, 2239–2245, (1985).
10. C. Tanford and J.G. Kirkwood, *J. Am. Chem. Soc.*, **79**, 5333–5339, (1957).
11. S.J. Shire, G.I.H. Hanania and F.R.N. Gurd, *Biochemistry*, **13**, 2967–2974, (1974).
12. J. Warwicker and H.C. Watson, *J. Mol. Biol.*, **157**, 671–679, (1982).
13. J. Warwicker, D. Ollis, F.M. Richards and T.A. Steitz, *J. Mol. Biol.*, **186**, 645–649, (1985).
14. R.J. Zauhar and R.S. Morgan, *J. Mol. Biol.*, **186**, 815–820, (1985).
15. N.K. Rogers and M.J.E. Sternberg, *J. Mol. Biol.*, **174**, 527–542, (1984).
16. J.R. Reitz and F.J. Milford, In *Foundations of Electromagnetic Theory*, p. 70, Addison-Wesley, Reading, Mass. (1967).
17. C.A. Brebbia, *Boundary Element Techniques in Computer-Aided Engineering*, NATO ASI Series, Martinus Nijhoff Publishers, (1984).
18. B.A. Dubrovin, A.T. Fomenko and S.P Novikov, *Modern Geometry–Methods and Applications. Part I*, Springer-Verlag, (1984).
19. O.C. Zienkiewicz, *The Finite Element Method*, 3rd Ed., McGraw-Hill, (1977).
20. J.E. Akin, *Application and Implementation of Finite Element Methods*, Academic Press, (1982).
21. M.L. Connolly, *J. Appl. Cryst.*, **18**, 499–505, (1985).
22. M.L. Connolly, *Molecular Surface Program*, Quantum Chemistry Program Exchange Bull. 1, p. 74, (1981).
23. W.S. Massey, *Algebraic Topology: An Introduction*, Springer-Verlag, (1967).
24. A. Rashin, R. Osman and R.J. Zauhar, in preparation.
25. R. Osman, S. Topiol and H. Weinstein, *J. Comp. Chem.*, **2**, 73–82, (1981).
26. K. Kamiya, M. Takamoto, Y. Wada, M. Fujino and M. Nishikawa, *J. Chem. Soc. Comm.*, 438–439, (1980).
27. G. Kartha, K.I. Varughese and S. Aimoto, *Proc. Natl. Acad. Sci.*, **79**, 4519–4522, (1982).
28. K. Hori, J.N. Kushick and H. Weinstein, *Ann. N.Y. Acad. Sci.*, in press, (1987).
29. A. Rashin and K. Namboodiri, in press.
30. B.R. Brooks, R.E. Bruccoleri, B.D. Olafson, D.J. States, S. Swaminathan, and M. Karplus, *J. Comp. Chem.*, **4**, 187–217, (1983).
31. H. Weinstein, D. Chou, S. Kang, C.L. Johnson, and J.P. Green, *Int. J. Quant. Chem.: Quant. Biol. Symp. No. 3*, 135–150, (1976).
32. S. Miertus, E. Scrocco, and J. Tomasi, *Chem. Phys.*, **55**, 117–129, (1981).
33. R. Constanciel, *Theor. Chim. Acta.*, **69**, 505–523, (1986).
34. P.B. Shaw, *Phys. Rev. A*, **32**, 2476–2487, (1985).